Production of radioactive ion beams using the in-flight technique

B. Harss,[a] R. C. Pardo, K. E. Rehm, F. Borasi,[b] J. P. Greene, R. V. F. Janssens, C. L. Jiang, J. Nolen, M. Paul,[c] J. P. Schiffer, R. E. Segel,[d] J. Specht, T. F. Wang,[e] P. Wilt, and B. Zabransky
Argonne National Laboratory, Argonne, Illinois 60439

(Received 4 August 1999; accepted for publication 5 November 1999)

Reactions with a heavy projectile incident on a light target can be used for the efficient in-flight production of secondary radioactive beams. An overview of this technique is given using data on ^{17}F beams produced via the $p(^{17}\mathrm{O}, ^{17}\mathrm{F})n$ and $d(^{16}\mathrm{O}, ^{17}\mathrm{F})n$ reactions. With primary ^{16,17}O beam currents of 100 pnA, intensities of up to 2×10^{6} ^{17}F/s on target were achieved. Using this beam, the $p(^{17}\mathrm{F},\alpha)^{14}\mathrm{O}$ reaction was measured. © *2000 American Institute of Physics.*
[S0034-6748(00)04002-8]

I. INTRODUCTION

Recently, there has been an increased interest in experiments with beams of short-lived radioactive nuclei addressing questions in areas of nuclear structure, nuclear astrophysics, and fundamental interactions. While measurements with tritium and ^{14}C had been performed in the past, a wider spectrum of radioactive beams has been used during the last ten years.[1,2]

Most of the shorter-lived radioactive beams are produced presently either via the isotope-separation-on line technique,[3–5] or the projectile-fragmentation method.[5] In the former, activities are produced with a driver accelerator or a reactor and are subsequently accelerated with another machine. In the latter, a primary heavy-ion beam of several tens of mega-electron-volts per nucleon is fragmented in a primary target and the resulting fragments, following electromagnetic selection, are then directly used for experiments. The in-flight technique is similar to the fragmentation method and has been used previously at various laboratories.[6–9] It provides isotopes close to stability without limitations due to lifetimes or chemical properties. In addition, it allows for an easy variation of the energy of the reaction products within a certain range and can be implemented in existing heavy-ion accelerators.[6–9] These advantages come at the price of the restrictions on beam quality and on ion species that can be produced.

The basic principle and parameters associated with the technique are described in Sec. II. Details of the production target are given in Sec. III. In Sec. IV, both a simple and a more elaborate beam transport scheme are described and a brief overview of the tuning process is given.

[a]Also at: Physics Department E12, Technische Universität München, Munich, Germany; electronic mail: rehm@anlphy.phy.anl.gov
[b]Also at: Northwestern University, Evanston, IL 60208.
[c]Present address: Hebrew University, Jerusalem, Israel.
[d]Present address: Northwestern University, Evanston, IL 60208.
[e]Present address: Lawrence Livermore National Laboratory, Livermore, CA 94550.

II. BASIC CONSIDERATIONS OF THE IN-FLIGHT PRODUCTION TECHNIQUE

In the in-flight production technique (Fig. 1), nuclear reactions in a ''primary'' or ''production'' target are used to transform heavy ions from an intense primary beam into the desired radioactive, secondary beam. For a beam of heavy ions incident on a low-mass target, the energies of the reaction products and of the incident ions are usually comparable. The challenge for the beam transport system (BTS) is to provide an efficient mechanism for suppressing the intense primary beam transmitted through the primary target while efficiently transporting the secondary beam.

In the following, the production of a secondary ^{17}F beam via the $d(^{16}\mathrm{O}, ^{17}\mathrm{F})n$ reaction is used as an example. The secondary particles are distributed in phase space with the characteristic parameters energy E, time t and angle θ with respect to the beam axis. Assuming radial symmetry, the particle position (x,y) in the plane perpendicular to the beam direction can be replaced by the radial distance r from the beam axis. Considering here only the transport of secondary ions in a single charge state, the yield function $Y(E,\theta,r,t)$ defines the distribution of $^{17}\mathrm{F}^{9+}$ ions in phase space at the *secondary* target. $Y(E,\theta,r,t)$ depends on the distribution of these ions after the *primary* target, described by the function $S(E,\theta,r,t)$ and on a transport operator $T(E,\theta,r,t)$ that selects and moves particles in phase space,[10] i.e., $Y=T\{S\}$. T represents a combination of a transport map and an acceptance function. To understand and predict Y, detailed knowledge of S and T, beyond characterization in terms of emittance, is required.

A. The source distribution *S* at the target

For a given primary beam energy, the total number of product particles S_{tot} in S is determined by the reaction cross section σ, together with the areal particle density τ_0 of the primary target and the primary beam current I_{beam}. To calculate S_{tot} one has to integrate over the energy dependent cross section $\sigma(E)$ as a function of the depth τ in the target, $\sigma(\tau)d\tau=\sigma(E)dEd\tau/dE$:

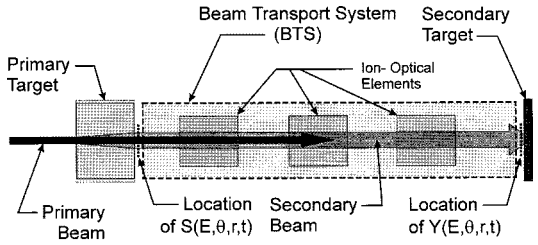

FIG. 1. Schematic of the in-flight production technique.

$$S_{\mathrm{tot}} = I_{\mathrm{beam}} \langle \sigma \tau_0 \rangle = I_{\mathrm{beam}} \int_0^{\tau_0} \sigma(E) dE \frac{d\tau}{dE}. \quad (1)$$

The stopping power $dE/d\tau$ in the target depends on all chemical components in the target layer in which reactions take place. Therefore, targets with a different chemical composition can result in different $\langle \sigma \tau_0 \rangle$ for the same primary beam energy and the same density τ_0. For slowly varying cross sections $\sigma(E)$ in the energy range of interest, S_{tot} is given by the product of $\tau_0 \sigma(E_{\mathrm{mid}}) I_{\mathrm{beam}}$, where E_{mid} is the energy at midtarget. Some total production cross sections for the $p(^{17}\mathrm{O}, ^{17}\mathrm{F})n$ (Refs. 11 and 12) and $d(^{16}\mathrm{O}, ^{17}\mathrm{F})n$ (Ref. 13) reactions are shown in Fig. 2.

1. The energy and angle dependence of $S(E,\theta)$

The energy and angle dependence of $S(E,\theta)$ is determined by the reaction kinematics, the differential reaction cross section $\sigma(E,\theta)$, the energy and angular spread of the incident ^{17}O beam, and the properties of the primary target. In general, no analytic expression for $S(E,\theta)$ can be given. Rather, it has to be calculated with a Monte Carlo simulation. The angle and energy spreads of the primary beam are usually small compared to the corresponding properties of the secondary beam and will therefore be neglected. Also, we will not elaborate on the fact that the $^{16}\mathrm{O}(d,n)^{17}\mathrm{F}$ reaction also populates the first excited state in ^{17}F at $E_x = 495$ keV.

First, the effect of the reaction kinematics on the dependence of S on E and θ will be considered. $S(E,\theta)$ for a ^{17}F beam produced via the $d(^{16}\mathrm{O}, ^{17}\mathrm{F})n$ reaction is shown in Fig. 3. In the laboratory system, for constant differential cross sections $d\sigma/d\Omega_{\mathrm{CM}}$, $S(E)$ is rectangular (solid line), while $S(\theta)$ exhibits a sharp peak at the maximum kinematic reaction angle θ_{max}. Unlike the angular distribution $d\sigma/d\Omega$, $S(\theta)$ has to be 0 at 0°, as a consequence of the differential angle ratio $d\theta/d\Omega$.

The effect of an angular distribution $d\sigma/d\Omega_{\mathrm{CM}}$ in the case of the $^{16}\mathrm{O}(d,n)^{17}\mathrm{F}$ reaction[14,15] is shown in Fig. 3 by the dashed lines. In this case, the cross section is forward peaked, which has a drastic impact on $S(E)$: a large portion of the reaction products is shifted towards higher energies. The impact on $S(\theta)$ is less pronounced: while the slope at small angles is steeper, most of the yield remains at large angles.

Straggling and energy losses in the thick primary target impact $S(E)$ and $S(\theta)$ by slowing and deflecting particles both before and after a reaction. The straggling in angle and energy varies with the square root of the target thickness,

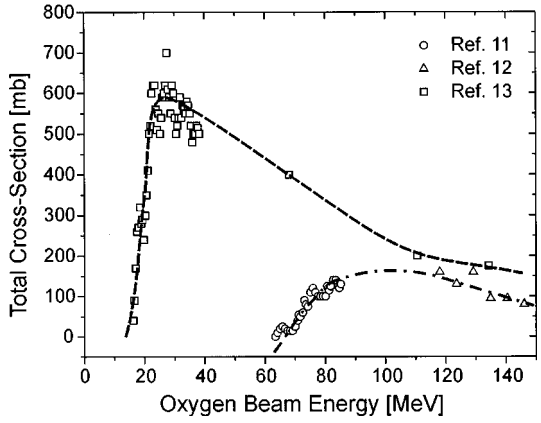

FIG. 2. Cross sections for the production of ^{17}F as a function of the beam energy using the $p(^{17}\mathrm{O}, ^{17}\mathrm{F})n$ and $d(^{16}\mathrm{O}, ^{17}\mathrm{F})n$ reactions. The data shown were taken from Refs. 11–13. The lines are drawn to guide the eye.

while the total energy loss is linear with the thickness. The Monte Carlo code TRIM[16] was used to simulate these effects. The dotted lines in Fig. 3 show the impact of these effects. To demonstrate these effects in isolation, $d\sigma/d\Omega_{\mathrm{CM}}$ was assumed to be constant. The distribution $S(E)$ is shifted as a whole to lower energies by the energy loss, with increased width and slight tails at high energies and a slow falloff at low energies. The sharp kinematic peak in $S(\theta)$ is broadened by particles scattered to smaller and, mostly, larger angles through small angle scattering. While the energy straggling is a relatively small effect compared to the width of $S(E)$ from the reaction kinematics, the small angle scattering can be of the same magnitude as the reaction opening angle.

Additional distortions of the kinematic distribution arise from several second order energy loss effects in the target. Reactions take place at different depths (and thus at different energies) in the target, creating particles with different opening cones and kinematic energy spreads. The specific stopping powers of the primary and the secondary beams and their energy dependence give rise to further modifications. Secondary particles produced near the first layer of the target have to travel through the rest of the material as a different species, experiencing a different stopping power than primary beam ions that react near the last layer of the target. At the same time, particles corresponding to the high energy (forward) solution lose less energy than those corresponding to the backward solution on the way out of the target. Especially for the backward solution, the kinematically defined relationship between angle and energy of the secondary beam particles is considerably weakened. Figure 4 shows the results of a Monte Carlo simulation of these effects for ^{17}F ions produced with a 75 MeV ^{16}O beam bombarding a 1.6 mg/cm^2 D_2 target.

2. The radius and time dependence of $S(r,t)$

For $S(r)$ and $S(t)$ the physical length of the production target is the most important factor. The width of $S(r)$ is given to a good approximation by the width of the radial distribution of the primary beam incident on the primary target plus a second term, which depends to first order linearly on the length of the target.

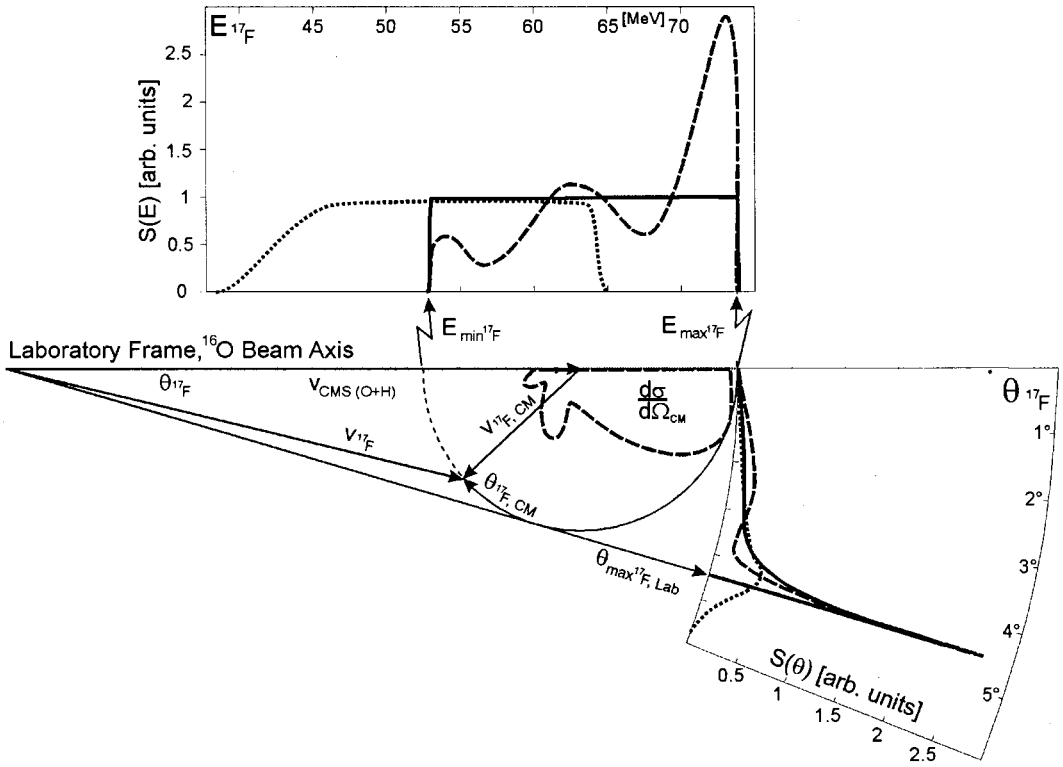

FIG. 3. $S(E)$ (top) and $S(\theta)$ (lower right) for ^{17}F from the ^{16}O$(d,n)^{17}$F reaction with a 67 MeV ^{16}O beam incident on a thin (0.01 mg/cm^2) and a thick (1.6 mg/cm^2), windowless deuterium target. The kinematic situation is shown along with the measured angular distribution $d\sigma/d\Omega_{\mathrm{CM}}$ (see Refs. 14 and 15) in the center of mass system. Solid lines: $d\sigma/d\Omega_{\mathrm{CM}}$ isotropic, thin target. Dashed lines: experimental $d\sigma/d\Omega_{\mathrm{CM}}$, thin target. Dotted lines: isotropic $d\sigma/d\Omega_{\mathrm{CM}}$ with energy loss and straggling effects, thick target.

For most purposes, the time dependence of $S(t)$ can be assumed to be identical to the time structure of the primary beam, if the target does not extend more than a few centimeters in the beam direction. In linear accelerator systems with radio frequency cavities and debunching capabilities, the primary beam has a sharply defined time structure with bunch lengths of 200 ps [full width at half maximum (FWHM)] or less. In such systems, especially in an arrangement with large angular acceptance, even a moderately extended target of a few centimeters can have a significant influence on $S(t)$. This arises from the different locations in the target, where particles of distributed energies are created and from the different masses and stopping powers of the primary and secondary beam ions. For particles emerging with the same energy from a moderately extended target, the time distribution width is given by a constant term of the order of the time width of the beam bunches plus a second term which, to a good approximation, increases linearly with the length of the target. A Monte Carlo simulation for the $d(^{16}\mathrm{O}, ^{17}\mathrm{F})n$ reaction in a 3.5 cm long D_2 target (1.6 mg/cm^2, 76 MeV ^{16}O beam, bunch width 0 ps) yielded a 60 ps bunch width for ^{17}F particles of 65 ± 0.25 MeV. With the same parameters, the ions emerging at 65 MeV from a 7 cm long target are distributed over 120 ps.

B. Transport considerations

Which part of the distribution $S(E,\theta,r,t)$ can actually be used depends on the beam quality required in the specific experiment (i.e., which E, θ, r, and t are acceptable) and on the ability of the BTS to move as much as possible of S into the acceptance window. Many nuclear physics experiments require a well-defined projectile energy and angle as well as a small beam spot. At the same time, the intense γ, x ray and neutron radiation at the production target potentially interferes with experimental arrangements. To physically separate the production target from the secondary target and to con-

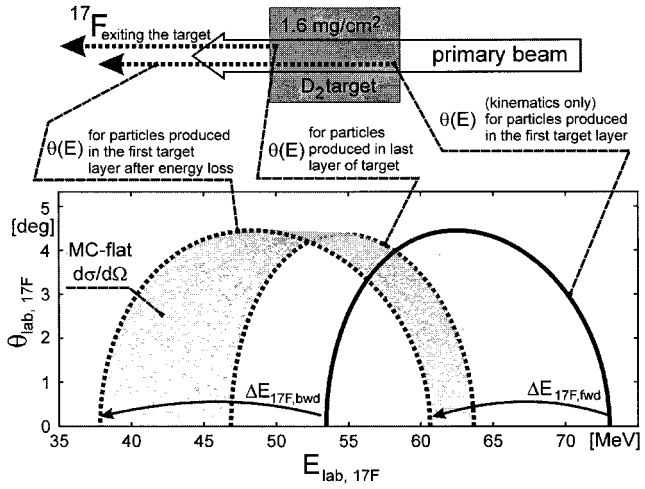

FIG. 4. The effect of the stopping power dependence on Z and E of an ion. The points are the results of a Monte Carlo simulation of the distribution of ^{17}F ions produced by a 75 MeV ^{16}O beam incident on a 1.6 mg/cm^2 deuterium target in a plot of θ vs E. The solid line indicates the kinematic curve for reactions in the first layer of the target. The dotted lines show the kinematic curves for particles generated in the first layer of the target after leaving the system and for particles generated in the last layer of the target.

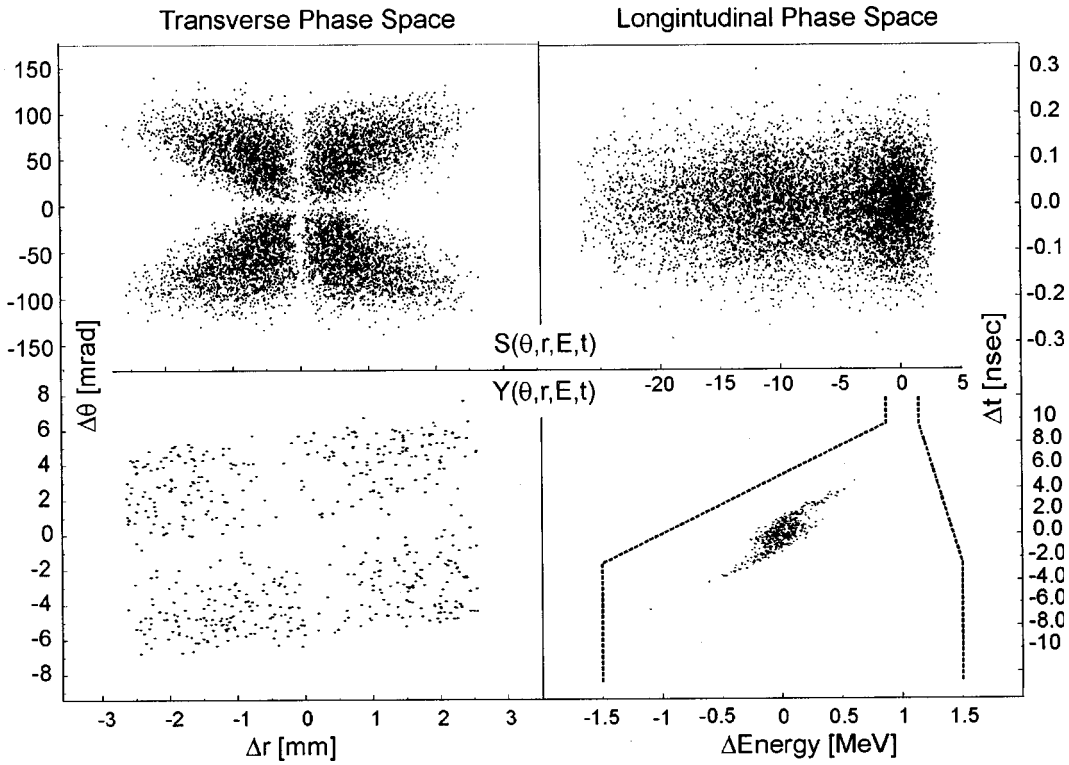

FIG. 5. Results of a Monte Carlo simulation of $S(s_{\mathrm{tot}}=10\,000)$ and Y for the setup used at Argonne. $^{17}F^{9+}$ ions are produced via the $d(^{16}O, ^{17}F)n$ reaction in a 1.6 mg/cm^2 D_2 gas target of 3.5 cm length with 1.9 mg/cm^2 HAVAR™ windows. The resulting $S(E,\theta,r,t)$ is shown in the two upper panels. S is then used as input for a radially symmetric transport code simulating the impact of a debunching resonator and of the beam-optical elements and apertures located in the 15 m long path between the primary and the secondary targets. The calculated transport efficiency is 5.9%.

trol the quality of the secondary beam, a number of optical components like solenoids, magnetic dipoles, and quadrupoles as well as debunching resonators can be used. The BTS and thus T in the equation $Y=T(S)$ moves particles in phase space from a location in S to a desired position in $Y(E,\theta,r,t)$.

The transport efficiency is defined as the fraction of all secondary particles whose parameters do not exceed the maximum allowed values for energy deviation $\Delta E_{\max}$, incident angle $\theta_{\max}$ and radius from the beam axis $r_{\max}$ on the secondary target. An upper limit on the transport efficiency can be obtained by comparing the product $\theta_{\max} r_{\max}$ with ϵ_{St}, the particle-normalized integral over r times θ of the source distribution S. $\varepsilon_{\mathrm{Sl}}$ is a quantity closely related to the transverse emittance of the product distribution, and we drop the distinction even though the phase space population is nonstatical. This integral is generally approximated by a sum over the properties of the particles created in a Monte Carlo simulation of the target. If the product $\theta_{\max}\times r_{\max}$ is smaller than ϵ_{St}, only part of the distribution S can be transported to the target station.

In rf accelerators, such as the ATLAS linac, there is a correlation between the velocity and the time of arrival of a particle at a given location in the BTS. This makes it possible to use a rf field to manipulate the longitudinal phase space and, thus, to reduce the energy spread of the reaction products. Limitations may arise from the achievable electric fields as well as from phase-space population. Numerically, this can be quantified by the normalized integral $\varepsilon_{\mathrm{Sl}}$ over the velocity deviation Δv times the deviation in time Δt of a certain particle from the centroid of the distribution, $\varepsilon_{\mathrm{Sl}}$ is closely related to the longitudinal emittance. The nonlinear effects of the rf field of the debunching resonator limit the maximal useful Δt, and therefore the minimum achievable ΔE. A limit of the transport efficiency can be obtained by comparing this ΔE with $\Delta E_{\max}$. In a full calculation of the total transport efficiency, phase-space related limits have to be combined with cuts arising from geometrical limitations in the BTS.

Figure 5 presents phase space diagrams for S (upper panels) and Y (lower panels) from a Monte Carlo calculation simulating a 1.6 mg/cm^2 D_2 gas target with a length of 3.5 cm and HAVAR™ entrance and exit windows of 1.9 mg/cm^2 thickness, using the $d(^{16}O, ^{17}F)n$ reaction. The 10 000 particles were generated and used as an input for the radially symmetric transport code LINRAY.[17] LINRAY simulated the effects of the 15 m long BTS between the primary and secondary target, including the debunching resonator and the optical elements as well as the geometric limitations that cause particle losses. Details of the ion-optical arrangement used at ATLAS are given in Sec. IV B. Thus, the program represented an approximation of the operator T, acting on S and calculating the expected Y that contained in this case 594 transported particles. The predicted transport efficiency of 5.9% for $^{17}F^{9+}$, which corresponds to an overall efficiency of 3.3% by accounting for the charge state distribution, is in reasonable agreement with the experimental observed $\sim$2.5%. The discrepancy is most likely caused by a reduction of the effective target thickness due to local heating of the D_2

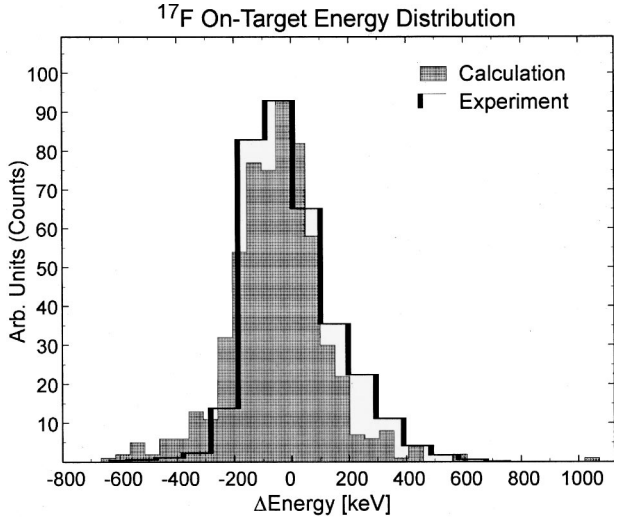

FIG. 6. Comparison between the simulated (hatched peak) and the observed (bold line) energy distributions $Y(E)$ on the secondary target, normalized to each other. The ^{17}F beam energy was 65 MeV.

gas along the beam axis and to the effects of quadrupole magnets which were modeled as radially symmetric lenses. It is interesting to note that the initial ''hole'' around $S(\theta=0,r=0)$ is preserved through the transport and translates into a similar feature in $Y(\theta,r)$.

The calculated energy distribution $Y(E)$ of the particles at the secondary target is compared with a measured distribution at 65 MeV in Fig. 6. For a realistic time width of $\Delta t=175$ ps for beam pulses incident on the gas cell target, an energy spread of ~400 keV (FWHM) is obtained, in good agreement with the experimental results. The experimental data show a slight tail on the high energy side (Fig. 6) which can be explained by a minor error in the rf phase of the bunching and debunching resonators, magnified by nonlinear effects in the rf field of the second resonator acting on a wide time distribution.

C. Typical requirements for reactions and production targets

For nuclear physics experiments, the usual requirements on the secondary beams are: high beam currents, a small beam spot, a small angle spread of the incoming projectiles, and a small energy spread. Based on the discussion in Secs. II A and II D, this translates into several general requirements for the efficient production of a given radioactive beam.

(1) In some cases, there is a choice between several reactions to produce the same secondary beam. Inverse reactions (heavy beams on light targets) such as inverse (p,n), (d,n), or (He,d) processes, preferably with negative Q values, should be chosen because of the narrow opening angle of the reaction products in the laboratory system. Forward-peaked differential cross sections are an advantage. Unfavorable values of these parameters for a specific reaction may be offset by a larger total cross-section.

(2) The angle and energy acceptance of the BTS should be as large as possible. Even for inverse reactions, the opening angles with respect to the beam axis are of the order of degrees and the energy spread is typically several mega-electron-volts.

(3) The size of the beam spot on the primary target should be small. In the case of an rf-based accelerator system with energy debunching capabilities, there should be a tight time focus at the primary target. These conditions minimize $\varepsilon_{\mathrm{St}}$ and $\varepsilon_{\mathrm{Sl}}$.

(4) The primary target should be designed to accept as large a beam current as possible.

(5) The primary target should induce as little small-angle straggling as possible.

(6) The primary target should be short. Since the width of $S(r)$ increases linearly with the physical length of the target, $\varepsilon_{\mathrm{St}}$ also increases linearly with this quantity.

(7) The primary target should have a high isotopic concentration in its active area. Because of the increased energy loss, compounds containing the target nucleus represent an inferior choice compared to isotopically pure material.

(8) Passive layers (windows), especially on the exit side of the target, should be as thin as possible. Thick windows induce increased small angle straggling, thus increasing $\varepsilon_{\mathrm{St}}$. They widen the energy distribution of the products, thereby increasing $\varepsilon_{\mathrm{Sl}}$. They also increase the energy loss of the primary beam, raising the total heat load on the target assembly. Increased straggling of the transmitted primary beam causes more secondary beam contamination due to energy tails of the primary beam.

III. THE PRIMARY GAS TARGET

From the requirements given in Sec. II C, hydrogen and helium are the preferred target materials. There are no He compounds, and H-rich compounds (e.g., CH_2) cannot withstand the thermal stress induced by intense primary beams. To circumvent these problems, stacks of three gas targets with metal windows were used in our experiments (Fig. 7, right).

As shown schematically in Fig. 7 (left), each target cell consists of a double-walled cylinder with 2.54 cm inner diameter, and a length of either 7.5 or 3.5 cm. The volume between the walls can be filled with a circulating cooling liquid (liquid nitrogen or a mixture of water and alcohol). The windows consisted of 1.9 mg/cm^2 HAVAR™ (a cobalt–chromium–nickel alloy) foils which were soldered to a stainless steel ring with an inner diameter of 1.3 cm. These rings were mounted on the gas cells using an indium gasket. The pressure in the gas cells ranged from 400 to 800 h Pa. A 100 pnA, 90 MeV ^{17}O beam deposits about 0.5 W in the entrance and the exit foils within a spot of 1–4 mm^2. Under these thermal, mechanical, and radiation stresses, the lifetime of the HAVAR-foils ranged from 6 to 80 h, depending on the beam spot size and the degree of cooling. The survival of these windows determined the maximum current used during the experiments. While defocusing the beam was not practical for reasons of transport efficiency, cooling the cells to liquid nitrogen temperature greatly increased the lifetime of the windows and resulted in targets with higher density at the same pressure. In order to eliminate the need for opening the

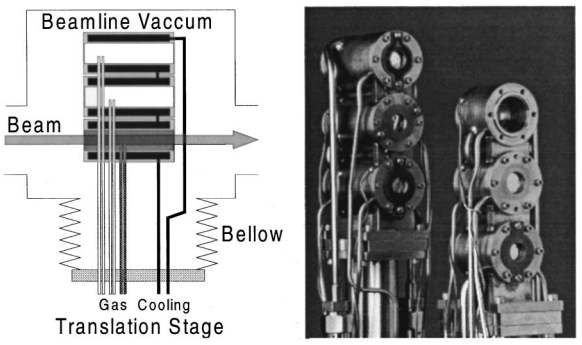

FIG. 7. Left: Schematic cross section of a set of three cylindrical gas targets with cooling and gas supply lines. Right: A photograph of two sets of three cells each, with length of 7.5 and 3.5 cm, respectively.

beam line system after a window failure, two sets of three gas cells were mounted on separate linear translation stages. More details on the cells, windows and the pressure regulation system will be given in a forthcoming publication.[18]

IV. PRODUCTION SETUPS AT ATLAS

A. Initial configuration

The gas cell was initially installed in front of the 22° bending magnet leading to the Enge split-pole spectrograph at the ATLAS accelerator at Argonne National Laboratory.[19] The angular acceptance for the secondary beam produced in the gas cell was limited to approximately 0.55° due to apertures in the beam line, thus severely reducing the transport efficiency of the ^{17}F beam. The acceptance was further reduced by the energy spread of the reaction products. For products of the $d(^{16}\mathrm{O},^{17}\mathrm{F})n$ reaction with a 90 MeV beam on the gas cell, the total transport efficiency of the beamline was estimated to be approximately 1% in this configuration. Including a 60% stripping efficiency into the 9^+ charge state of ^{17}F, the maximum possible transmission efficiency was expected to be 0.6%.

In this configuration,[20] ^{17}F beams with energies between 55–100 MeV were produced. The $d(^{16}\mathrm{O},^{17}\mathrm{F})$ reaction was used for ^{17}F energies below 60 MeV while the $p(^{17}\mathrm{O},^{17}\mathrm{F})n$ reaction was preferred for secondary energies above 60 MeV. The average ^{17}F beam intensity was 700 $(\mathrm{s\,pnA})^{-1}$ and corresponded to a beam transport efficiency of approximately 0.3%. With a primary ^{16}O beam of up to 250 pnA, rates of 2×10^5 ^{17}F/s on the secondary target were achieved. The beam spot on the secondary target was 0.8 cm^2 in area, limited by a circular aperture. The principal contaminants of the ^{17}F beam were energy-degraded primary beam particles, i.e., ^{17}O or ^{16}O ions with the same magnetic rigidity. Their intensities varied between 10% and 50% of the total secondary beam, depending on the actual tune of the accelerator. A representative spectrum obtained with this system is shown in Fig. 8.

B. Improved configuration

A new production and transport configuration used in recent experiments[21] is shown in Fig. 9. The production target has been moved upstream by approximately 5 m, placing

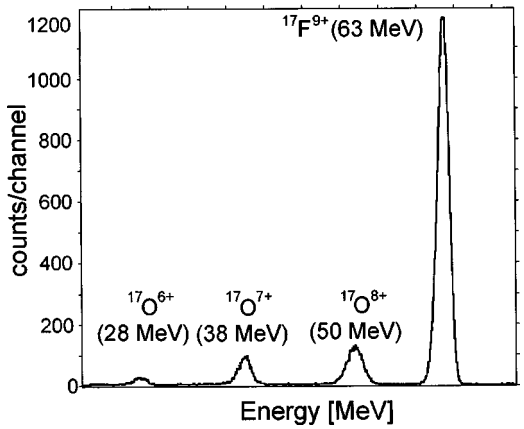

FIG. 8. Energy spectrum of a ^{17}F beam produced with the $p(^{17}\mathrm{O},^{17}\mathrm{F})n$ reaction using the first generation setup. The secondary ^{17}F beam and oxygen contaminants from primary beam tails with the same magnetic rigidity are clearly seen.

it between two existing ATLAS superconducting resonators and just in front of a newly installed 2.2 T superconducting solenoid which was installed to increase the angular acceptance. It was mounted in such a way that it could be moved over a 0.63 m distance along the beam axis. This allows optimal placement of the device for different kinematical conditions. This geometry is a compromise between the need for a sufficiently small beam envelope, as the ^{17}F particles travel through the 2.54 cm diameter collimator of the second rf cavity, and the need to minimize the divergence of the ions so that as much secondary beam as possible can be captured and refocused by the optical elements in the spectrograph beam line. The distance between the gas cell and the target used in the experiment is about 15 m, corresponding to a time-of-flight of 550 ns for 65 MeV ^{17}F ions.

A superconducting ''bunching'' resonator located 10 m upstream from the production target was used to provide a time focus of the primary beam at the gas cell. This minimized the longitudinal emittance of the secondary beam. The resulting strong energy-time correlation after a 3 m drift from the target to the second rf cavity was then employed to reduce the energy spread with the second resonator. Experimentally, we found that using only the second ''debunching'' resonator increased the transmitted beam by about

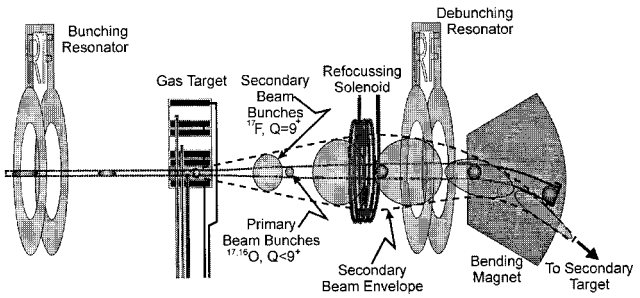

FIG. 9. Improved production configuration showing the impact of an added superconducting solenoid and a pair of resonators on both the primary and secondary beam bunches. While the solenoid focuses the beam in transverse direction, the resonator pair reduces the energy spread of the reaction products and moves more of them into the momentum acceptance of the bending magnet.

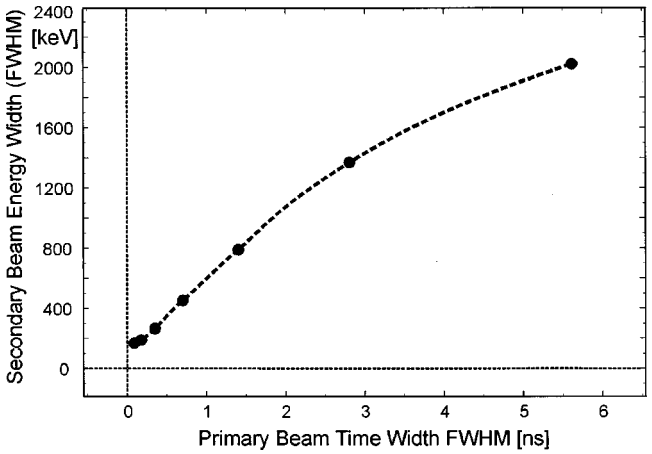

FIG. 10. Calculated achievable energy spread as a function of the time width of the beam pulses on the primary target. The dashed line is drawn to guide the eye.

10%–20%, but that using both resonators yielded an improvement by a factor of 2 in beam current compared to optimization with only the superconducting solenoid. In this configuration, the total transport efficiency was measured to be 2.5%, yielding a maximum intensity of 2×10^6 ^{17}F/s on the secondary target. At the same time, the energy resolution of the beam was improved from ~1.2 MeV FWHM to better than 400 keV (Fig. 6). It is worth noting that this 400 keV energy spread translates into a spread of only 23 keV in the center of mass for the $p(^{17}\mathrm{F},^{14}\mathrm{O})\alpha$ reaction which is of astrophysics interest.[21] The importance of achieving a time waist for the final ^{17}F energy spread is shown by the calculation presented in Fig. 10. Details of the experiment and the beam normalization can be found in Ref. 21.

The phase of the second rf cavity can also be adjusted to change the energy of the $^{17}F^{9+}$ beam over a range of approximately ±5 MeV, while still maintaining a small energy spread. This feature allows to choose the production energy based partially on the secondary beam yield rather than on the required secondary energy. Also, scanning excitation functions can be achieved by using the second rf cavity.

The beam backgrounds observed in the new configuration were qualitatively different from the backgrounds in the original setup. While in most cases the primary beam leaking through was reduced well below the 10% level, products of parasitic reactions in the primary target became relatively more important (e.g., ^{17}O from the $d(^{16}\mathrm{O},^{17}\mathrm{O})p$ reaction). The total contamination of the beam was between 10% and 50%.

C. Tuning

Since the process of tuning the radioactive secondary beam onto the target is nontrivial, a brief overview of the procedure used in the experiments is given here. In a first step, a weak primary beam (e.g., $^{16}O^{8+}$) transmitted through the gas target was tuned to the secondary target position. The small-angle straggling caused a considerable divergence, allowing to optimize the setting of the beamline components (solenoid and quadrupole doublets) in a configuration similar to that required for the transport of $^{17}F^{9+}$.

In the second step, all magnetic elements after the primary target were scaled from the magnetic rigidity $B\rho = p/Q$ of the primary beam (e.g., $^{16}O^{8+}$ at 70 MeV) to the rigidity of the secondary beam (e.g., $^{17}F^{9+}$ at 65 MeV). The primary beam intensity was then increased to a current of 100 pnA and a 1:1000 attenuator was inserted after the 22° bending magnet. This procedure reduced the expected ^{17}F rate on the secondary target to $\sim10^3$ pps, allowing the use of the focal plane counter in the split pole spectrograph positioned at 0° to directly analyze the beam with respect to mass, Z and energy. The ^{17}F yield measured at the focal plane was subsequently optimized by fine tuning the various elements of the BTS. For this purpose, the output of the energy amplifier and the same signal digitized with a custom built multichannel analyzer were passed to the accelerator control room. It should be noted that the increased beam current in the final step of tuning is crucial because heating effects change the effective target density on the beam axis and thereby alter $S(E)$.

TABLE I. Data for secondary beams produced at ATLAS with the in-flight technique.

Beam	Production reaction	Secondary energy+ half width at half maximum [MeV]	Intensity (pps per pnA primary beam)	Bakcgrounds [fract. of total beam (%)]
^{25}Al	$^{24}\mathrm{Mg}(d,n)^{25}\mathrm{Al}$	204 ±0.8	1×10^3	^{24}Mg(50) ^{25}Mg(<1)
^{25}Al	$^{25}\mathrm{Mg}(p,n)^{25}\mathrm{Al}$	180 ±1.5	2×10^3	^{25}Mg(20) ^{24}Mg(<1)
^{21}Na	$^{20}\mathrm{Ne}(d,n)^{21}\mathrm{Na}$	113 ±0.5	4×10^3	^{20}Ne(50) ^{21}Ne(<0.1) ^{18}F(<0.1)
^{21}Na	$^{21}\mathrm{Ne}(p,n)^{21}\mathrm{Na}$	113 ±0.3	8×10^3	^{21}Ne(40) ^{20}Ne(<0.1)
^{17}F	$d(^{16}\mathrm{O},^{17}\mathrm{F})n$	40–65 ±0.2	2×10^4 (Intensity achieved 2×10^6)	^{17}O(10) ^{16}O(10–30)
^{17}F	$p(^{17}\mathrm{O},^{17}\mathrm{F})n$	60–110 ±0.2	2×10^4 (Intensity achieved 2×10^6)	^{17}O(10–30) ^{14}N(2)

V. DISCUSSION AND OUTLOOK

^{17}F was the first beam of short-lived ions produced and successfully used in physics experiments[20,21] at ATLAS. Recently, beams of ^{21}Na and ^{25}Al have been developed as well. Initial tests with (d,n) and a (p,n) reactions were performed. A brief overview of the results is shown in Table I.

This technique for producing beams of short-lived nuclei can be applied to many other isotopes. In the mass range below ^{56}Ni, there are more than 50 radioactive beams that can be produced by (p,n), (d,n), or (p,d) reactions. The secondary beam intensities depend on the parameters discussed above and on the efficiency of the mechanism to separate the primary from the secondary beam. The available primary beam intensity and the ability of the primary target to withstand thermal and radiation stresses pose specific technical limits. For light elements ($Z \leqslant 10$), the gas cell target can withstand currents in excess of 100 pnA. However, the increasing energy loss for heavier primary beams will become a limiting factor for the secondary beam intensities that can be achieved. A possible improvement is the use of gas targets with plasma windows[22] which would eliminate this restriction. Tests of such a system are presently being performed.

An alternative mechanism to separate the primary and secondary beams is the use of a shadow bar as described in Ref. 6. Such a device in combination with the selection of the magnetic rigidity $B\rho$ should provide cleaner secondary beams, especially in systems with higher nuclear charge Z. A development effort to build a remotely controlled shadow bar with cooling capability and variable solid angle coverage is under consideration.

ACKNOWLEDGMENTS

This work was supported by the US D.O.E., Nuclear Science Division, under Contract Nos. W-31-109-ENG-38 (ANL), DE-FG02-98ER-41086 (NU) and by a University of Chicago/Argonne National Laboratory Collaborative Grant. B. H. wants to thank Professor Hans-Joachim Körner (Technische Universität München) for support of his Ph.D. thesis at Argonne National Laboratory.

[1] Proceedings of the Fourth International Conference on Radioactive Nuclear Beams, Omiya, Japan, 3 June 1996, edited by S. Kubono, T. Kobayashi, and I. Tanihata, Nucl. Phys. A **616**, 1c (1997), and references therein.
[2] Proceedings of ENAM98 (Exotic Nuclei and Atomic Masses), edited by B. M. Sherrill, D. J. Morrissey, and C. N. Davids [AIP Conf. Proc. **455**, 1 (1998), and references therein].
[3] H. L. Ravn, Nucl. Instrum. Methods Phys. Res. B **70**, 107 (1992).
[4] D. Darquennes *et al.*, Phys. Rev. C **42**, R804 (1990).
[5] G. Münzenberg, H. Geissel, and C. Schneidenberger, Proceedings of the 13th International Conference on Electromagnetic Isotope Separators and Techniques Related to their Applications (EMIS-13), Bad Dürkheim, Germany, 23–27 September 1996 [Nucl. Instrum. Methods. Phys. Res. **126**, 1 (1997), and references therein].
[6] R. C. Haight *et al.*, Nucl. Instrum. Methods Phys. Res. **212**, 245 (1983).
[7] T. Yamaya *et al.*, Nucl. Instrum. Methods Phys. Res. B **70**, 374 (1992).
[8] A. Ozawa *et al.*, RIKEN-AF-NP-236 (unpublished).
[9] J. J. Kolata, A. Morsad, X. J. Kong, R. E. Warner, F. D. Becchetti, W. Z. Liu, D. A. Roberts, and J. W. Jänecke, Nucl. Instrum. Methods Phys. Res. B **40**, 503 (1989); J. J. Kolata *et al.*, Phys. Rev. Lett. **81**, 4580 (1998).
[10] Hereafter, for simplicity, $S(E,\theta,r,t)$, $T(E,\theta,r,t)$, and $Y(E,\theta,r,t)$ are simply labeled as S, T, and Y, unless their dependence on certain parameters is specifically addressed. In this case, these parameters are given in parentheses.
[11] J. K. Bair, Phys. Rev. C **8**, 120 (1973).
[12] J. D. Anderson *et al.*, Phys. Rev. **177**, 1416 (1969).
[13] W. Gruhle, Nucl. Phys. A **186**, 257 (1972).
[14] S. T. Thronton, Nucl. Phys. A **137**, 531 (1969).
[15] C. J. Oliver *et al.*, Nucl. Phys. A **127**, 567 (1969).
[16] J. F. Ziegler and J. P. Biersack, *The Stopping Power of Ions in Solids* (Pergamon, New York, 1985).
[17] R. C. Pardo and K. W. Shepard (unpublished).
[18] B. Harss *et al.* (unpublished).
[19] B. Harss *et al.*, Proceedings of the XVIII International Linear Accelerator Conference, Geneva, Switzerland, CERN 96-07 **2**, 496 (1996).
[20] K. E. Rehm *et al.*, Phys. Rev. Lett. **81**, 3341 (1998).
[21] B. Harss *et al.*, Phys. Rev. Lett. **82**, 3964 (1999).
[22] A. Hershcovitch, Phys. Plasmas **5**, 2130 (1998).